metals

MDPI

Article

Submerged Dissimilar Friction Stir Welding of AA6061 and AA7075 Aluminum Alloys: Microstructure Characterization and Mechanical Property

Akbar Heidarzadeh [1], Mousa Javidani [2,*], Mohammadreza Mofarrehi [2], Amir Farzaneh [3] and X.-Grant Chen [2,*]

[1] Department of Materials Engineering, Azarbaijan Shahid Madani University, Tabriz 53714-161, Iran; ac.heydarzadeh@azaruniv.ac.ir
[2] Department of Applied Science, University of Québec at Chicoutimi, Saguenay, QC G7H 2B1, Canada; mohammadreza.mofarrehi1@uqac.ca
[3] Department of Materials Engineering, University of Maragheh, Maragheh 83111-55181, Iran; amir.frz@maragheh.ac.ir
* Correspondence: Mousa_Javidani@uqac.ca (M.J.); XGrant_Chen@uqac.ca (X.-G.C.)

Abstract: The possibility of underwater dissimilar friction stir welding of AA6061 and AA7075 aluminum alloy was explored to overcome the problem of hardness loss in different microstructural zones. Optical microscopy and electron backscattered diffraction were employed to characterize the microstructure of the joint. Vickers hardness measurements were conducted on the cross-section of the joint to evaluate the mechanical strengths. The results showed that the microstructure of the AA7075 side had undergone the same mechanisms as those occurring during conventional friction stir welding. In the case of the AA6061 side, in addition to typical restoration mechanisms, the grain subdivision was observed. The AA7075 side had finer grains compared to the AA6061 side, which may be related to the different morphology and size of precipitates. Moreover, friction stir welding caused a reduction in the hardness values in all the microstructural areas compared to those of corresponding base materials. For example, it caused a reduction in the hardness of a thermomechanically affected zone from 105 HV to 93 HV in the AA6061 side, and from 187 HV to 172 HV in the AA7075 side. The underwater media improved the overall hardness values in thermo-mechanically affected zones (13% reduction in hardness) compared to those reported in literature (57% reduction in hardness).

Keywords: friction stir welding; underwater welding; microstructure; aluminum alloys

Citation: Heidarzadeh, A.; Javidani, M.; Mofarrehi, M.; Farzaneh, A.; Chen, X.-G. Submerged Dissimilar Friction Stir Welding of AA6061 and AA7075 Aluminum Alloys: Microstructure Characterization and Mechanical Property. *Metals* **2021**, *11*, 1592. https://doi.org/10.3390/met11101592

Academic Editor: Daixiu Wei

Received: 17 September 2021
Accepted: 4 October 2021
Published: 7 October 2021

1. Introduction

Friction stir welding (FSW) is a suitable solid-state process to join dissimilar metals and alloys. The microstructures of dissimilar materials subjected to FSW usually consist of five distinct zones, namely an onion structure-like stirred zone (SZ), thermo-mechanically affected zone (TMAZ), and heat-affected zone (HAZ), as well as base metals (BMs) [1,2]. However, the microstructures of the dissimilar FSWed joints are composed of complicated microstructural regions, driven by complex material movement. As the material flow plays a major role in the dissimilar material welding, the microstructural evolution strongly depends on the welding process variables. The microstructure evolving in the SZ of dissimilar welds may vary from lamellar structure to complex intercalated lamellar structure [3–5]. If the weld parameters are inappropriate, then the intermixing of the materials does not take place sufficiently. On the other hand, the appropriate selection of all process parameters results in excellent material mixing on both sides (advancing side (AS) and the retreating side (RS)) of the joint and produces a sound weld with a symmetric weld zone. It is worth noting that selecting the right welding parameters such as tool geometry [6] and welding

media [7] plays a main role in determining the optimum final mechanical properties of the FSWed joints of metals and alloys.

To improve the overall performance of the FSWed joints, the microstructural evolution during the process must be well assessed [2,8]. Therefore, the microstructural characteristics of dissimilar FSWed Al alloys have recently attracted great research attention [9–16]. Raturi et al. [9] studied the effect of secondary heating on material behavior during FSW of AA6061 and AA7075 dissimilar aluminum alloys, in which the hardness of the joints decreased along the weld cross-section when the additional heat was employed. Zhang et al. [10] analyzed the grain structure and texture evolution of dissimilar AA2024 and AA7075 FSWed joints. They reported that the mean grain size and recrystallization amount were reduced at higher traverse speeds. In another study, Raturi et al. [11] explored the mechanical and corrosion properties of dissimilar FSWed AA7075 and AA2014 joints. They revealed that the traverse speed and tool pin profile had a significant influence on tensile strength, whereas the tool pin had the maximum effect on strength. Niu et al. [12] studied the cyclic deformation properties of FSWed AA2024 and AA7075 aluminum alloy joints. They disclosed that after the cyclic deformation of 500 cycles at a total strain amplitude of 0.5%, the strength of the dissimilar joints resumed mainly to that of AA2024 alloy. Zhang et al. [13,14] demonstrated that the low corrosion resistance was presented in the thermo-mechanically affected zones compared to the base materials in AA2024 and AA7075 joint produced by FSW. They have also mentioned that the joining direction [15] and tool rotational speed [16] could considerably affect the mechanical and corrosion behavior of FSWed AA2024 and AA7075 joints.

From the viewpoint of microstructural evolution, such as the FSW joints of similar alloys, the SZ in dissimilar cases undergoes extensive grain refinement, producing fine grain microstructures, while the TMAZ is usually composed of a large and elongated grain structure [17,18]. The final grain size of the SZ depends on the initial grain size of the base metals and the welding variables. Grain refinement in SZ of the FSWed joints is primarily driven by shear deformation process and dynamic recrystallization [17,18]. For instance, according to Srinivasan et al. [19], a very fine and recrystallized grain structure was developed in the SZ of FSWed dissimilar AA6056-AA7075 joints. Despite the extensive grain refinement, a grain size variation across the SZ was also observed, which could be attributed to the initial grain sizes of the respective base materials. Recently, Niu et al. [20] observed highly inhomogeneous microstructures evolved across the FSWed AA5083-AA2024 joint. They conducted a comprehensive electron backscattered diffraction (EBSD) investigation across the joint cross-section and realized the tilted and elongated grains in the TMAZ and fine grains in the SZ.

In addition to low heat input welding processes such as laser beam welding (LBW) [21], the applied cooling media (e.g., underwater condition) can improve the mechanical properties of FSWed joints by optimizing the weld microstructure [22–24]. The underwater condition compared to other types of welding methods can also result in improved microstructure and mechanical properties [25–28], which confirms the advantages of submerged processes. Although some research works on dissimilar FSW joint of Al alloys such as AA2024-7075 [29], AA6061-7075 [5], AA6082-2024 [30], AA7075-5083 [31], and AA5086-6061 [32] can be found in literature, investigations on microstructural evolution of the underwater FSWed joints of 6xxx and 7xxx Al alloys are very limited [33]. In this study, the microstructural characteristics and hardness evolution of different zones in underwater dissimilar FSWed AA6061-AA7075 joints were investigated.

2. Materials and Methods

AA6061-T6 and AA7075-T6 Al plates with a length of 10 cm, a width of 5 cm, and a thickness of 5 mm were underwater FSWed. The employed water media was at room temperature. The chemical composition and hardness of base materials are summarized in Table 1. A hot work H13 tool composed of a shoulder with a diameter of 15 mm and a pin with a height of 4.6 mm and a diameter of 5 mm was employed for FSW at a

traverse speed of 100 mm/min, a rotational speed of 400 mm/min, and a plunge depth of 0.1 mm to produce one dissimilar joint. The samples for microstructure observation were cut from the joint cross-section perpendicular to the FSW direction at the middle of the produced joint (with a 5 cm distance from the joint's beginning point). After being subjected to the standard grinding and polishing procedure, the samples were etched in Barker's reagent (5 mL HBF4 48% in 200 mL H_2O), then anodized at 40 V for 90 s. The microstructural characteristics were subsequently examined using polarized light optical microscopy (OM). Electron backscattering diffraction (EBSD) analysis was carried out in a scanning electron microscope (SEM, JEOL JSM-6480LV, JEOL Ltd., Tokyo, Japan) with a step size of 0.5 µm, and the corresponding data were processed using Channel 5 analysis software. The grain and subgrain boundaries were identified based on the misorientation angles, as the low-angle boundaries (LABs: 2–5°, marked by white line), medium-angle boundaries (MABs: 5–15°, blue line) and high-angle boundaries (HABs: >15°, black line). The Vickers microhardness (HV) test was conducted by a NG-1000 CCD machine (NextGen Material Testing, Inc., Vancouver, BC, Canada) on the joint cross-section with a constant force (load) of 25 g and a dwell time of 20 s.

Table 1. Chemical composition and hardness of base materials used in this study.

Alloy	Chemical Composition (wt. %)									Hardness (Hv)
AA6061	Mg	Si	Fe	Cu	Cr	Zn	Ti	Mn	Al	105
	1.01	0.62	0.35	0.24	0.17	0.12	0.12	0.07	Bal.	
AA7075	Mg	Si	Fe	Cu	Sn	Zn	Ni	Mn	Al	187
	2.50	0.40	0.50	1.60	0.20	5.60	0.03	0.30	Bal.	

3. Results

The inverse pole figure (IPF) maps of the base materials (BMs) are shown in Figure 1. Both of the BMs were in T6 condition and contained elongated grains originating from the preceding rolling process. The cross-sectional macrostructure of the joint is presented in Figure 2a. Similar to the other dissimilar FSWed Al alloys [1,34], the macrostructure was composed of the BMs (AA6061 and AA7075), heat affected zones (HAZs), TMAZs, and SZ. For the sake of brevity, this study focused specifically on TMAZs and interfacial areas in SZ to elaborate on the main microstructural mechanisms of grain structure evolution.

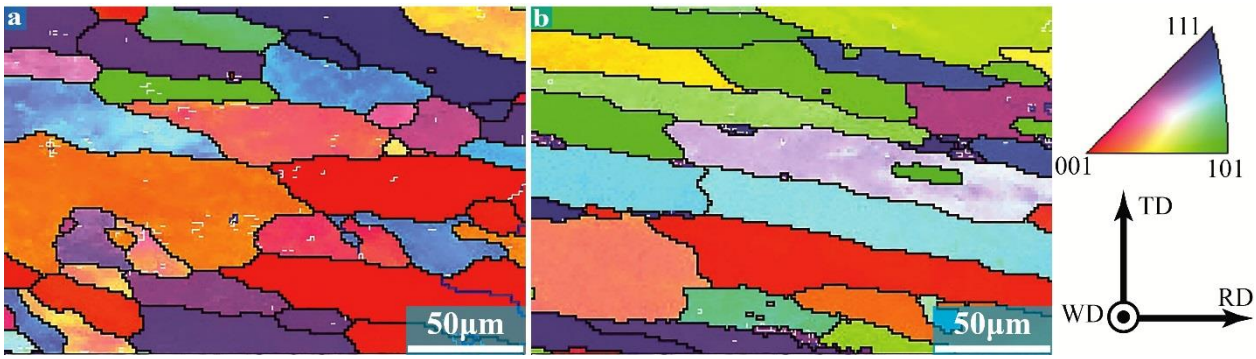

Figure 1. IPF maps of the BMs: (**a**) AA6061, and (**b**) AA7075. WD, TD, and RD are the abbreviations of welding, traverse, and rolling directions, respectively.

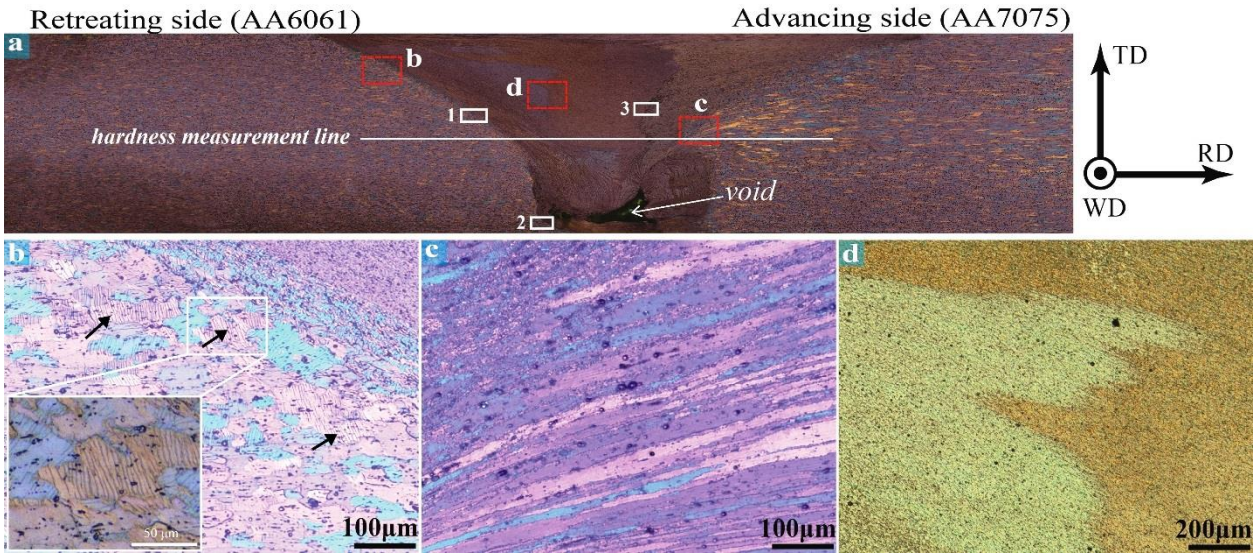

Figure 2. (**a**) Cross-sectional macrostructure of the joint. (**b**–**d**) the microstructures of the areas identified in (**a**); (**b**) grain subdivision in TMAZ of AA6061 (the inset image in left-bottom corner is an enlarged view of the area identified by white rectangle); (**c**) elongated large grains in TMAZ of AA7075 without subdivision process; (**d**) the interfacial area at the center of the joint. White rectangles (1–3 numbered) refer to the EBSD scan areas. The white line belongs to the hardness measurement line. The white arrow refers to a void formed in the cross-section of the joint.

The OM images of TMAZs and interfacial areas are shown in Figure 2b–d. The grains in TMAZ of the AA6061 side, which are elongated to some extent, are shown in Figure 2b. Some microscopic parallel lines, indicated by the black arrows and enlarged in the inset of Figure 2b, are observed in the grain interiors. They can be the sign of grain subdivision. To the best of our knowledge, this type of microstructure in TMAZ of AA6061 has never been reported previously; thus, it has been discussed in more detail using IPF maps. On the other hand, the TMAZ of the AA7075 side (Figure 2c) exhibited a typical microstructure containing elongated grains similar to those reported in literature [35]. Moreover, from OM image of the interfacial zone in SZ (Figure 2d), the SZ contained fine grains due to the occurrence of dynamic recrystallization (DRX). As he grain sizes of this region could not be well-identified by OM, the IPF map of this area was also analyzed and discussed in more detail in the following section.

The IPF and grain boundary maps of TMAZ and the transition zone (to SZ) in the AA6061 side are shown in Figure 3a,b. Figure 4 illustrates the IPF map of the interfacial area in the SZ, which indicates two different grain sizes in a dissimilar joint of Al alloys under the same deformation condition. The hardness profile along with the corresponding indentation plan in the middle line on the cross-section of the joint are presented in Figure 5. Furthermore, to characterize the variation of the hardness values across the joint and to correlate with the corresponding microstructures, some OM images were taken from specific locations (identified by a–f in the hardness profile), which are shown in Figure 6.

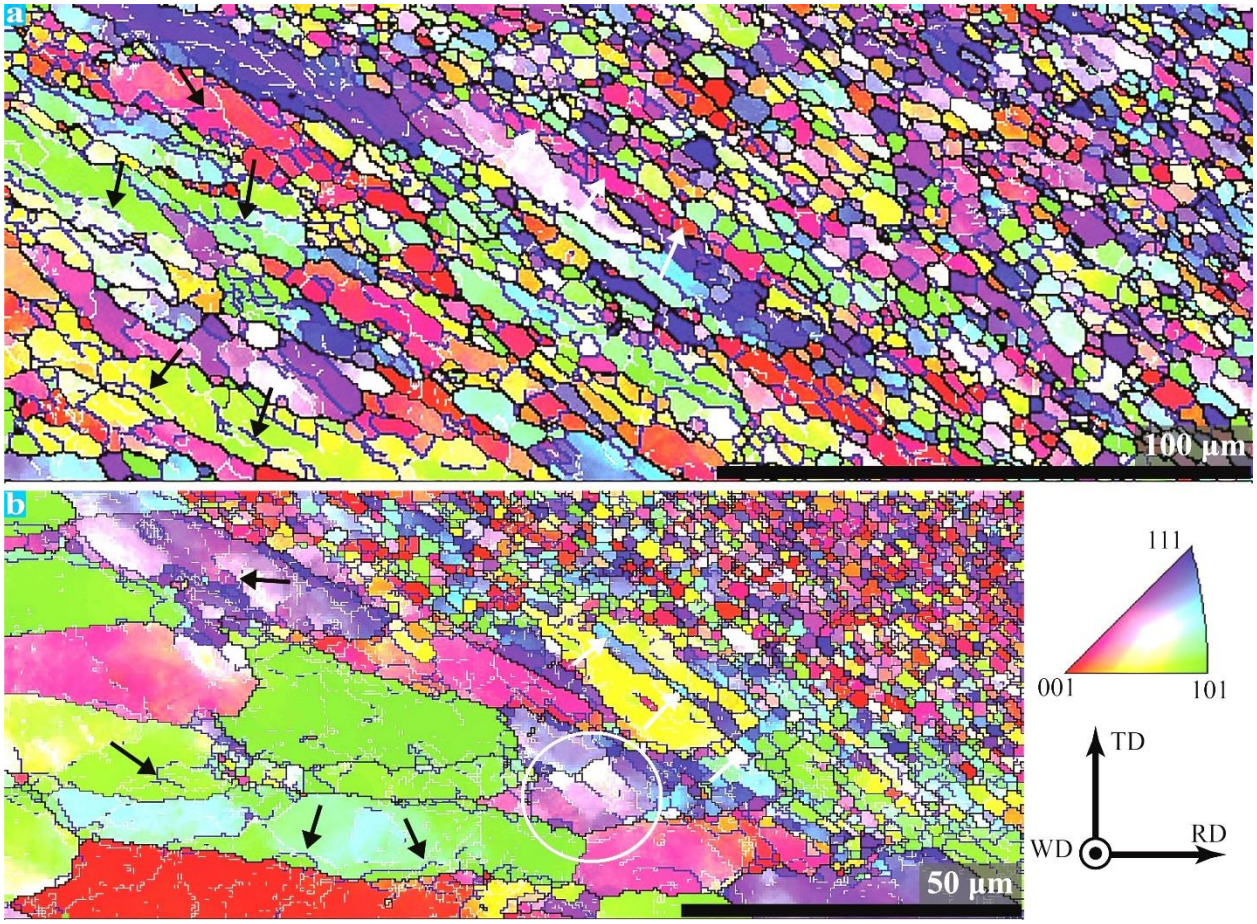

Figure 3. IPF maps of different areas in TMAZ of AA6061: (**a**) rectangle 1 in Figure 2a, and (**b**) rectangle 2 in Figure 2a. Black and white arrows refer to CDRX and GDRX mechanisms, respectively. The white circle indicates a grain in which the subdivision mechanism has occurred.

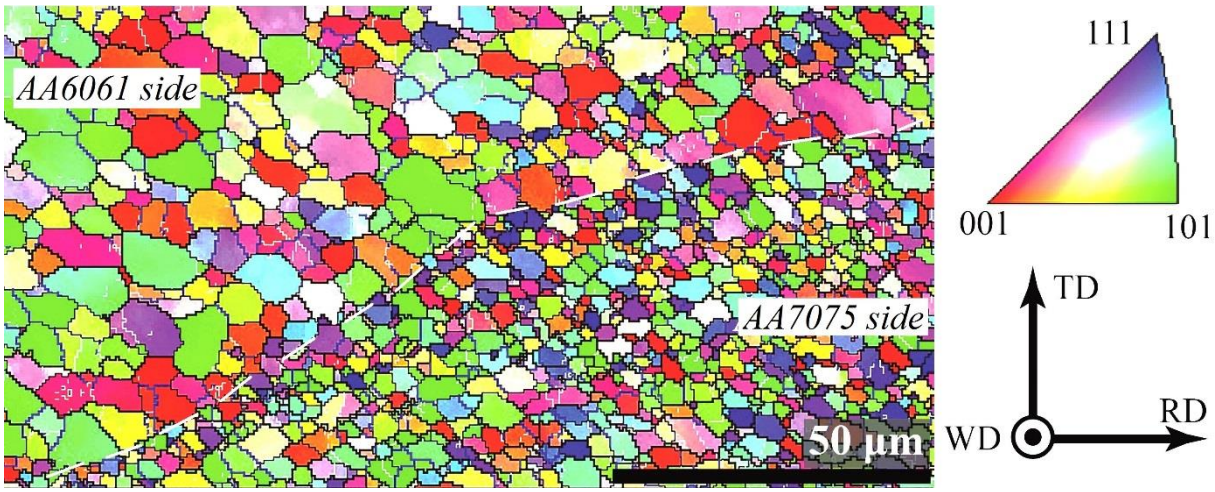

Figure 4. The IPF map of interfacial area in SZ indicated by the white rectangle 3 in Figure 2a. The interface between AA6061 and AA7075 alloys are drawn by a dashed line.

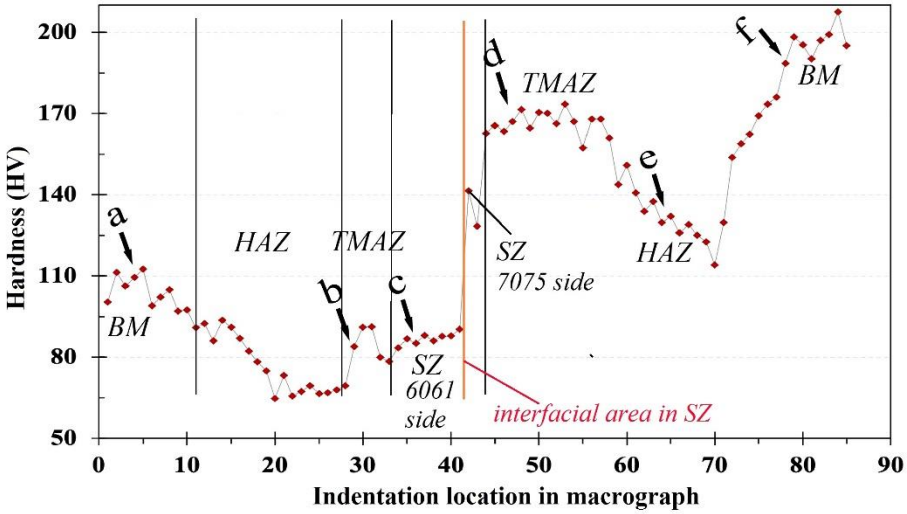

Figure 5. Hardness profile along the line indicated by white line in Figure 2a. (**a**–**f**) refer to area that their corresponding microstructures are illustrated in Figure 6. The different microstructural zones are also divided in the AA6061 side by black vertical lines.

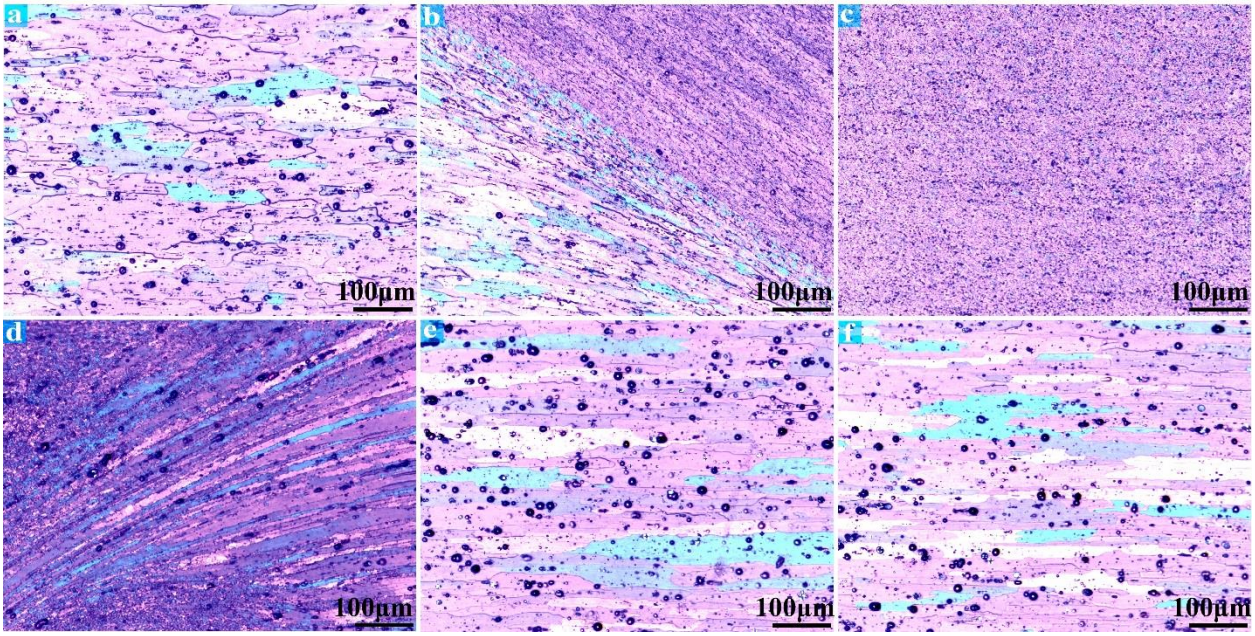

Figure 6. OM images of the areas (**a**–**f**) indicated on the hardness profile (Figure 5). c belongs to the AA6061 side in SZ.

4. Discussion

Different microstructural mechanisms during the FSW process, which are involved in the grain structure evolution, are mainly driven by both the process heat input and the applied deformation. Dynamic recovery (DRV) occurs during the hot deformation of materials with high stacking fault energies (SFEs) in which restoration mechanisms such as the formation of LABs happen to generate new subgrains inside the deformed old grains. As it can be observed in Figure 3a,b, a large number of LABs and MABs were formed in the TMAZ/transition-zone of AA6061 alloy, which implies the occurrence of DRV. The black arrows in Figure 3a,b indicate the zones in which the transition of LABs→MABs→HABs takes place. This type of transition is the sign of continuous DRX (CDRX) after DRV [34]. By further straining after the DRV initiation, mobile dislocations move towards the LABs; intersecting LABs by the dislocations enhances misorientation angle. This process changes LABs to MABs, which are subsequently followed by transforming MABs to HABs in a

similar manner. Finally, equiaxed grains surrounded by HABs appear in the microstructure as can be seen in the upper-right corner of Figure 3b. Thus, one of the dominating mechanisms in this study was CDRX. Moreover, very close to SZ in TMAZ, some grains were elongated to very narrow thicknesses almost equal to the diameter of DRXed grains in SZ, which is the sign of geometrically DRX (GDRX) grains and are indicated by the white arrows in Figure 3. The occurrence of GDRX requires a very high level of strain that is available near the SZ.

The grain subdivisions, observed in TMAZ of AA6061 and indicated by the black arrows in Figure 2b, are most likely the traces of slip bands inside individual grains. The comparison between Figures 2b and 3b indicates that these subdivision mechanisms do not change the crystallographic orientation of grains in TMAZ far from the SZ since they have not been observed in IPF maps. However, at the areas near to SZ, where the amount of strain is more than areas far from SZ (indicated by white circle in Figure 3b), they appear in IPF maps. It indicates that by increasing the amount of strain, the required strain for the onset of grain subdivision mechanism has been provided, then it changes the orientation of the divided parts of an individual grain, and hence the new grains can be generated. It is notable grain subdivision mechanism is frequently reported to happen during the deformation of cubic metals with high stacking fault energies [36,37].

Another point of interest, which is shown in Figure 4, is the formation of different grain sizes of AA6061 and AA7075 in SZ, where the AA7075 had finer grain sizes relative to AA6061. The formation of different grain sizes at the same deformation condition, i.e., at the SZ, can be due to the presence of precipitates with different compositions, sizes, and morphologies in the microstructure of AA6061 and AA7075 alloys. It seems that the presence of more alloying elements in the chemical composition of AA7075, relative to AA6061, causes the formation of more precipitates which consequently affect the restoration mechanisms during FSW. The possible mechanisms that can be affected by precipitates are particle stimulated nucleation (PSN) and the Zener pinning effect. The larger precipitates (usually larger than 1 μm) act as the nucleation sites for DRX by PSN mechanisms, whereas the finer precipitates pin the grain boundaries during grain growth step after DRX (the Zener pinning effect), and hence they lead to the formation of finer grain sizes [34,38]. The formation of different grain sizes in SZ is also reported by other investigators [5,33]; however, the real origin of this behavior has not been disclosed yet, and it is within the scope of the future research plan of the authors.

Correlation between the hardness values (Figure 5) with the corresponding microstructures (Figure 6) reveals some interesting points. AA7075 (point f in Figures 5 and 6) and AA6061 (point a in Figures 5 and 6) BMs had different hardness values. The higher hardness values of AA7075 were the reason for placing it at the AS of the joint during FSW. Thus, the other parameters such as rotational speed, traverse speed, tool plunge depth, tool offset, etc., should be optimized to obtain a defect-free joint, which was not the aim of this study. The void type defect formed in the cross-section of the joint has been indicated by a white arrow in Figure 2a. The other point is the same trend of the hardness profile on both the AS and RS. For example, the TMAZs (points b and d in Figures 5 and 6) had lower hardness compared to the BMs, which can be due to partial DRX in these areas and coarsening of precipitates [13,14]. In addition, the hardness profile in Figure 5 confirms the existence of interfacial area between the AA6061 and AA7075 sides in SZ (Figure 4). The higher hardness values of the AA7075 side in SZ can be due to finer grain sizes and more precipitates compared to those in the AA6061 side. It seems that FSW has not caused the complete intermixing of both dissimilar sides in SZ, but it resulted in a joint by mixing them in the interfacial zone.

It is worth noting that the loss in hardness values in the microstructural zones of the FSWed joints, such as TMAZ and HAZ, is a problematic issue [34], which changes these areas to the weakest points of the joints. From Figure 5, the drop in hardness values from BMs to TMAZs (from 105 HV to 93 HV in the AA6061 side, and from 187 HV to 172 HV in the AA7075 side) is not problematic compared to those reported during

conventional FSW [5,34]. For instance, a drop in hardness value from about 110 HV (AA6061 BM) to 70 HV (AA6061 TMAZ) i.e., a reduction of about 57% has been reported during dissimilar FSW of AA60601-7075 alloys [5]. However, in this study, this reduction in hardness value is approximately about 13 % (from 105 HV to 93 HV). This improvement in the hardness of TMAZ can be related to the lower heat input generated during an underwater FSW process; a lower process heat input can result in different metallurgical phenomena, such as preventing the growth and dissolution of precipitates, inhibiting the grain growth, and recovery of dislocations [25–33]. On the other hand, HAZ (point e in Figures 5 and 6) had the lowest hardness values on both sides, which can be due to the dissolution or coarsening of precipitates and/or grain growth. Moreover, the hardness value in the SZ is lower than that of the TMAZs, which is due to complete DRX (point c in Figures 5 and 6). Therefore, it can be concluded that using underwater media can overcome the problem of hardness loss in TMAZ of the precipitation hardening Al alloy joint, which can be employed instead of the costly and time-consuming treatments such as post-heat treatments [4] and cyclic deformation [12].

5. Conclusions

The microstructural evolution during underwater dissimilar FSW of AA6061 and AA7075 Al alloys was investigated, and the main conclusions are drawn as follows.

(1) The microstructural mechanisms during grain structure formation in the AA7075 side were the same as those occurring during conventional FSW of AA7075 plates. However, in the case of the AA6061 side, in addition to DRV, CDRX and GDRX, other restoration mechanisms such as grain subdivision were observed, which had not been reported in previous studies.

(2) The AA7075 consisted of finer grains compared to AA6061 in SZ, which can be related to the difference in their metallurgical characteristics (e.g., morphology and size of precipitates).

(3) There was a variation in the hardness profile across the joint. The HV values, which were the highest in BMs, were reduced in the TMAZs relative to BMs. FSW caused a reduction in hardness of TMAZ from 105 HV to 93 HV in the AA6061 side, and from 187 HV to 172 HV in the AA7075 side. The submerged FSW enhanced the hardness values in TMAZs (13% reduction in hardness) compared to those reported in literature (57% reduction in hardness). The HAZs presented the lowest HV values across the joint.

(4) The outcome of this study can be used to understandthe fundamentals of grain structure evolution during underwater submerged dissimilar FSW of Al alloys.

Author Contributions: A.H.: methodology, investigation, formal analysis, writing—original draft; M.J.: conceptualization, methodology, formal analysis, writing—review and editing; M.M.: conceptualization, methodology, validation, review and editing; A.F.: conceptualization, validation, review and editing; X.-G.C.: conceptualization, validation, review and editing, Project administration. All authors have read and agreed to the published version of the manuscript.

Funding: This research was funded by of the Natural Sciences and Engineering Research Council of Canada (NSERC) under the Grant No. CRDPJ 514651-17.

Acknowledgments: The authors would like to acknowledge the financial support of the Natural Sciences and Engineering Research Council of Canada (NSERC) under the Grant No. CRDPJ 514651-17.

Conflicts of Interest: The authors declare no conflict of interest.

Nomenclature

FSW	Friction Stir Welding
SZ	Stirred Zone
TMAZ	Thermo-Mechanically Affected Zone
HAZ	Heat-Affected Zone
BMs	Base Metals
AS	Advancing Side
RS	Retreating Side
EBSD	Electron Backscattered Diffraction
LBW	Laser Beam Welding
OM	Optical Microcopy
SEM	Scanning Electron Microscope
LABs	Low-Angle Boundaries
MABs	Medium-Angle Boundaries
HABs	High-Angle Boundaries
HV	Vickers Microhardness
IPF	Inverse Pole Figure
DRV	Dynamic Recovery
SFEs	Stacking Fault Energies
DRX	Dynamic Recrystallization
CDRX	Continuous Dynamic Recrystallization
GDRX	Geometrically Dynamic Recrystallization
PSN	Particle Stimulated Nucleation

References

1. Meng, X.; Huang, Y.; Cao, J.; Shen, J.; dos Santos, J.F. Recent Progress on Control Strategies for Inherent Issues in Friction Stir Welding. *Prog. Mater. Sci.* **2021**, *115*, 100706. [CrossRef]
2. Paidar, M.; Ojo, O.O.; Moghanian, A.; Karapuzha, A.S.; Heidarzadeh, A. Modified friction stir clinching with protuberance-keyhole levelling: A process for production of welds with high strength. *J. Man. Proc.* **2019**, *41*, 177–187. [CrossRef]
3. Bozkurt, Y.; Salman, S.; Çam, G. Effect of welding parameters on lap shear tensile properties of dissimilar friction stir spot welded AA 5754-H22/2024-T3 joints. *Sci. Tech. Weld. Join.* **2013**, *18*, 337–345. [CrossRef]
4. İpekoğlu, G.; Çam, G. Effects of Initial Temper Condition and Postweld Heat Treatment on the Properties of Dissimilar Friction-Stir-Welded Joints between Aa7075 and Aa6061 Aluminum Alloys. *Metall. Mater. Trans. A* **2014**, *45*, 3074–3087. [CrossRef]
5. Guo, J.F.; Chen, H.C.; Sun, C.N.; Bi, G.; Sun, Z.; Wei, J. Friction Stir Welding of Dissimilar Materials between Aa6061 and Aa7075 Al Alloys Effects of Process Parameters. *Mater. Design (1980–2015)* **2014**, *56*, 185–192.
6. Janeczek, A.; Tomków, J.; Fydrych, D. The Influence of Tool Shape and Process Parameters on the Mechanical Properties of Aw-3004 Aluminium Alloy Friction Stir Welded Joints. *Materials* **2021**, *14*, 3244. [CrossRef] [PubMed]
7. Memon, S.; Tomków, J.; Derazkola, H.A. Thermo-Mechanical Simulation of Underwater Friction Stir Welding of Low Carbon Steel. *Materials* **2021**, *14*, 4953. [CrossRef] [PubMed]
8. Calogero, V.; Costanza, G.; Missori, S.; Tata, M.E. A Weldability Study of Al–Cu–Li 2198 Alloy. *Metallurgist* **2014**, *57*, 1134–1141. [CrossRef]
9. Raturi, M.; Bhattacharya, A. Microstructure and Texture Correlation of Secondary Heating Assisted Dissimilar Friction Stir Welds of Aluminum Alloys. *Mater. Sci. Eng. A* **2021**, *825*, 141891. [CrossRef]
10. Zhang, C.; Huang, G.; Liu, Q. Quantitative Analysis of Grain Structure and Texture Evolution of Dissimilar Aa2024/7075 Joints Manufactured by Friction Stir Welding. *Mater. Today Commun.* **2021**, *26*, 101920. [CrossRef]
11. Raturi, M.; Bhattacharya, A. Mechanical Strength and Corrosion Behavior of Dissimilar Friction Stir Welded Aa7075-Aa2014 Joints. *Mater. Chem. Phys.* **2021**, *262*, 124338. [CrossRef]
12. Niu, P.L.; Li, W.Y.; Chen, D.L. Tensile and Cyclic Deformation Response of Friction-Stir-Welded Dissimilar Aluminum Alloy Joints: Strain Localization Effect. *J. Mater. Sci. Technol.* **2021**, *73*, 91–100. [CrossRef]
13. Zhang, C.; Huang, G.; Liu, Q. Research on Local Corrosion Behavior of Thermo-Mechanically Affected Zone in Dissimilar Aa2024/7075 Friction Stir Welds. *Intermetallics* **2021**, *130*, 107081. [CrossRef]
14. Zhang, C.; Huang, G.; Cao, Y.; Zhu, Y.; Huang, X.; Zhou, Y.; Li, Q.; Zeng, Q.; Liu, Q. Microstructure Evolution of Thermo-Mechanically Affected Zone in Dissimilar Aa2024/7075 Joint Produced by Friction Stir Welding. *Vacuum* **2020**, *179*, 109515. [CrossRef]
15. Zhang, C.; Huang, G.; Cao, Y.; Zhu, Y.; Li, W.; Wang, X.; Liu, Q. Microstructure and Mechanical Properties of Dissimilar Friction Stir Welded Aa2024-7075 Joints: Influence of Joining Material Direction. *Mater. Sci. Eng. A* **2019**, *766*, 138368. [CrossRef]

16. Zhang, C.; Cao, Y.; Huang, G.; Zeng, Q.; Zhu, Y.; Huang, X.; Li, N.; Liu, Q. Influence of Tool Rotational Speed on Local Microstructure, Mechanical and Corrosion Behavior of Dissimilar Aa2024/7075 Joints Fabricated by Friction Stir Welding. *J. Manuf. Process.* **2020**, *49*, 214–226. [CrossRef]
17. Fonda, R.W.; Bingert, J.F.; Colligan, K.J. Development of Grain Structure During Friction Stir Welding. *Scr. Mater.* **2004**, *51*, 243–248. [CrossRef]
18. Shen, C.; Zhang, J.; Ge, J. Microstructures and Electrochemical Behaviors of the Friction Stir Welding Dissimilar Weld. *J. Environ. Sci.* **2011**, *23*, S32–S35. [CrossRef]
19. Srinivasan, P.B.; Dietzel, W.; Zettler, R.; Dos Santos, J.F.; Sivan, V. Effects of Inhibitors on Corrosion Behaviour of Dissimilar Aluminium Alloy Friction Stir Weldment. *Corros. Eng. Sci. Technol.* **2007**, *42*, 161–167. [CrossRef]
20. Niu, P.L.; Li, W.Y.; Vairis, A.; Chen, D.L. Cyclic Deformation Behavior of Friction-Stir-Welded Dissimilar Aa5083-to-Aa2024 Joints: Effect of Microstructure and Loading History. *Mater. Sci. Eng. A* **2019**, *744*, 145–153. [CrossRef]
21. Malikov, A.G.; Orishich, A.M. Laser Welding of the High-Strength Al–Cu–Li Alloy. *Int. J. Adv. Manuf. Technol.* **2018**, *94*, 2217–2227. [CrossRef]
22. Aghajani Derazkola, H.; Eyvazian, A.; Simchi, A. Submerged Friction Stir Welding of Dissimilar Joints between an Al-Mg Alloy and Low Carbon Steel: Thermo-Mechanical Modeling, Microstructural Features, and Mechanical Properties. *J. Manuf. Process.* **2020**, *50*, 68–79. [CrossRef]
23. Luo, X.C.; Zhang, D.T.; Cao, G.H.; Qiu, C.; Chen, D.L. Multi-Pass Submerged Friction Stir Processing of Az61 Magnesium Alloy: Strengthening Mechanisms and Fracture Behavior. *J. Mater. Sci.* **2019**, *54*, 8640–8654. [CrossRef]
24. Eyvazian, A.; Hamouda, A.; Tarlochan, F.; Derazkola, H.A.; Khodabakhshi, F. Simulation and Experimental Study of Underwater Dissimilar Friction-Stir Welding between Aluminium and Steel. *J. Mater. Res. Technol.* **2020**, *9*, 3767–3781. [CrossRef]
25. Tomków, J.; Fydrych, D.; Wilk, K. Effect of Electrode Waterproof Coating on Quality of Underwater Wet Welded Joints. *Materials.* **2020**, *13*, 2947. [CrossRef]
26. Moreno-Uribe, A.M.; Bracarense, A.Q.; Pessoa, E.C.P. The Effect of Polarity and Hydrostatic Pressure on Operational Characteristics of Rutile Electrode in Underwater Welding. *Materials* **2020**, *13*, 5001. [CrossRef] [PubMed]
27. Tomków, J.; Janeczek, A.; Rogalski, G.; Wolski, A. Underwater Local Cavity Welding of S460n Steel. *Materials* **2020**, *13*, 5535. [CrossRef] [PubMed]
28. Tomków, J. Weldability of Underwater Wet-Welded Hsla Steel: Effects of Electrode Hydrophobic Coatings. *Materials* **2021**, *14*, 1364. [CrossRef] [PubMed]
29. Chen, Y.J.; Li, Y.J.; Walmsley, J.C.; Dumoulin, S.; Gireesh, S.S.; Armada, S.; Skaret, P.C.; Roven, H.J. Quantitative Analysis of Grain Refinement in Titanium During Equal Channel Angular Pressing. *Scr. Mater.* **2011**, *64*, 904–907. [CrossRef]
30. Cavaliere, P.; De Santis, A.; Panella, F.; Squillace, A. Effect of Welding Parameters on Mechanical and Microstructural Properties of Dissimilar Aa6082–Aa2024 Joints Produced by Friction Stir Welding. *Mater. Des.* **2009**, *30*, 609–616. [CrossRef]
31. Kalemba-Rec, I.; Kopyściański, M.; Miara, D.; Krasnowski, K. Effect of Process Parameters on Mechanical Properties of Friction Stir Welded Dissimilar 7075-T651 and 5083-H111 Aluminum Alloys. *Int. J. Adv. Manuf. Technol.* **2018**, *97*, 2767–2779. [CrossRef]
32. Jamshidi Aval, H.; Serajzadeh, S.; Kokabi, A.H. Thermo-Mechanical and Microstructural Issues in Dissimilar Friction Stir Welding of Aa5086–Aa6061. *J. Mater. Sci.* **2011**, *46*, 3258–3268. [CrossRef]
33. Dong, J.; Zhang, D.; Luo, X.; Zhang, W.; Zhang, W.; Qiu, C. Ebsd Study of Underwater Friction Stir Welded Aa7003-T4 and Aa6060-T4 Dissimilar Joint. *J. Mater. Res. Technol.* **2020**, *9*, 4309–4318. [CrossRef]
34. Heidarzadeh, A.; Mironov, S.; Kaibyshev, R.; Çam, G.; Simar, A.; Gerlich, A.; Khodabakhshi, F.; Mostafaei, A.; Field, D.P.; Robson, J.D.; et al. Friction Stir Welding/Processing of Metals and Alloys: A Comprehensive Review on Microstructural Evolution. *Prog. Mater. Sci.* **2020**, *117*, 100752. [CrossRef]
35. Mishra, R.S.; Ma, Z.Y. Friction Stir Welding and Processing. *Mater. Sci. Eng. R Rep.* **2005**, *50*, 1–78. [CrossRef]
36. Bay, B.; Hansen, N.; Hughes, D.A.; Kuhlmann-Wilsdorf, D. Overview No. 96 Evolution of F.C.C. Deformation Structures in Polyslip. *Acta Metall. Et Mater.* **1992**, *40*, 205–219. [CrossRef]
37. Hughes, D.A.; Hansen, N. High Angle Boundaries Formed by Grain Subdivision Mechanisms. *Acta Mater.* **1997**, *45*, 3871–3886. [CrossRef]
38. Humphreys, F.J.; Hatherly, M. *Recrystallization and Related Phenomena*, 2nd ed.; Elsevier: Amsterdam, The Netherlands, 2004.